Geophysical Journal International

Geophys. J. Int. (2014) **196,** 1189–1206
Advance Access publication 2013 November 29

doi: 10.1093/gji/ggt454

Surface wave phase velocities of the Western United States from a two-station method

Anna Foster, Göran Ekström and Meredith Nettles

Department of Earth and Environmental Sciences, Columbia University, 61 *Route* 9*W, Palisades, NY* 10964*, USA. E-mail: afoster@ldeo.columbia.edu*

Accepted 2013 November 5. Received 2013 November 1; in original form 2013 July 16

SUMMARY

We calculate two-station phase measurements using single-station measurements made on USArray Transportable Array data for surface waves at periods from 25 to 100 s. The phase measurements are inverted for baseline Love and Rayleigh wave phase velocity maps on a 0.5° × 0.5° grid. We make estimates of the arrival angle for each event at each station using a mini array method similar to beamforming, and apply this information to correct the geometry of the two-station measurements. These corrected measurements are inverted for an additional set of phase velocity maps. Arrival angles range from 0° to ±15°, and the associated corrections result in local changes of up to 4 per cent in the final phase velocity maps. We select our preferred models on the basis of the internal consistency of the measurements, finding that the arrival-angle corrections improve the two-station phase measurements, but that Love wave arrival-angle estimates may be contaminated by overtone interference. Our preferred models compare favourably with recent studies of the phase velocity of the Western United States. The corrected Rayleigh wave models achieve greater variance reduction than the baseline Rayleigh wave models, and the baseline Love wave models, which are more difficult to obtain, are robust and could be used in conjunction with the Rayleigh wave models to constrain radially anisotropic earth structure.

Key words: Surface waves and free oscillations; Seismic tomography; Wave propagation; North America.

Downloaded from http://gji.oxfordjournals.org/ at Columbia University on February 8, 2014

1 INTRODUCTION

The Western United States has a varied and complex tectonic history, with areas undergoing extension and subduction juxtaposed with cratonic regions of long-lived stability. The present-day structure of the crust and mantle results in elastic heterogeneity, which can be mapped using seismic methods and used to inform our understanding of the geology. Because of their sensitivity, surface waves are particularly useful for investigating the crust and upper mantle, where many of the signatures of geodynamic processes are expected to be found. In addition, the depth of surface wave sensitivity varies with frequency, providing good constraints on the depth of velocity anomalies.

The USArray Transportable Array (TA) program is an ongoing observational experiment, designed to obtain high-quality broad-band seismic data spanning the continental United States, with the goal of improving knowledge of continental structure and tectonic processes. Four hundred three-component broad-band seismometers are installed with 70-km grid spacing for 2-yr time periods, beginning on the West Coast of the United States and progressively stepping eastward (see www.usarray.org, last accessed 21 November 2013). With the data coverage provided by the TA, it is now possible to map properties of surface wave propagation in a uniform manner across the western part of the country. High-quality phase velocity maps can then be used to constrain models of 3-D structure, as well as to predict earthquake signals and back-project recorded signals to learn more about the earthquake source.

A wide variety of methods have been used to make measurements of the phase or phase velocity of surface waves in North America. Single-station methods measure the phase accumulated over the entire ray path from source to receiver, must account for source effects and are sensitive to errors in earthquake location (e.g. Trampert & Woodhouse 1995). Studies using single-station measurements to constrain the structure of North America include Lee & Solomon (1979), van der Lee & Nolet (1997), Godey *et al.* (2003), van der Lee & Frederiksen (2005), Marone *et al.* (2007), Nettles & Dziewoński (2008), Pollitz & Snoke (2010) and Yuan *et al.* (2011).

Multiple-station methods require two or more receivers, all recording the same event for earthquake-based techniques, and often impose specific geometric constraints related to the station alignment with the ray path. With the availability of high-quality TA data, the amount of seismic data has increased dramatically, making multiple-station methods a popular tool over the last several years. Many new and innovative techniques have been developed, including ambient noise tomography (e.g. Shapiro *et al.* 2005), Eikonal tomography (Lin *et al.* 2009), wave gradiometry (Liang & Langston 2009) and multiple plane wave tomography (Forsyth & Li 2005; Yang & Forsyth 2006). These studies have achieved good

© The Authors 2013. Published by Oxford University Press on behalf of The Royal Astronomical Society.

resolution when applied to the TA data set, and results appear to be consistent.

Two-station methods have not yet been applied to this data set. Such methods span the observational gap between ambient noise tomography, typically performed over very short interstation paths and at short periods, and teleseismic single-station studies with long paths and at longer periods. A two-station method reduces sensitivity to the source location and mechanism, an advantage over single-station methods. Because the measurement suppresses the influence of structure outside of the interstation path, which can be short compared with the teleseismic path, these measurements should help constrain small-scale structure in a phase velocity model inversion.

A limitation of two-station methods is the restriction that the interstation path lie approximately on the great circle from the earthquake source. However, the grid-like design of the TA ensures many available paths and dense and even coverage of the region. It is also often assumed that the wave travels as a ray along the great circle path from source to receiver. As early as the 1950s, it was recognized that heterogeneous velocity structure results in off great circle arrivals (Evernden 1954). Indeed, contours of single-station phase measurements on TA data show visible variations in the wave front, evidence that deviations in the ray path result in off great circle arrivals. This deviation from the great circle path is defined as the arrival angle, and several arrival-angle measurement methods have been developed (e.g. Vidale 1986; Lerner-Lam & Park 1989; Laske *et al.* 1994; Larson & Ekström 2002). In a previous study using a two-station method, Brisbourne & Stuart (1998) used measurements of arrival angle to discard data from events that did not arrive sufficiently aligned with the great circle path, limiting the authors to a small number of events. Because of TA data coverage, this issue can instead be addressed by measuring the arrival angle and combining it with the interstation phase observation.

All of the previously mentioned phase measurement methods can, in principle, be applied to obtain both Love and Rayleigh wave measurements. Challenges arise when making Love wave measurements, however; greater noise on the horizontal components and a less-dispersed wave packet can prevent high-quality measurement in some circumstances. Because of this, few Love wave phase velocity maps from TA data have been published; among these are phase velocity maps from ambient noise tomography at periods of 8–20 s from Lin *et al.* (2008), and examples at 60 and 150 s from Yoshizawa & Ekström (2010).

Love and Rayleigh waves have different sensitivity to vertical and horizontal shear velocity due to their differing particle motions. By making measurements of both wave types, radial anisotropy can be constrained, providing information about rock fabric and mantle flow patterns (e.g. Becker *et al.* 2003). Previous studies of radial anisotropy in the Western United States have indicated the presence of regional heterogeneity. Studies of upper-mantle radial anisotropy in North America have observed laterally varying strengths of 1–5 per cent (Nettles & Dziewoński 2008; Yuan *et al.* 2011). Studies using surface wave measurements from ambient noise in the Western United States have also found radial anisotropy in the middle or mid-to-lower crust, with strengths up to 5 per cent (Bensen *et al.* 2009; Moschetti *et al.* 2010). Thus, radial anisotropy is a significant factor in velocity structure studies, and increased knowledge of this parameter by the mapping of Love and Rayleigh wave dispersion has direct applications to geodynamic interpretations.

In this paper, we derive two-station phase measurements from a large data set of single-station phase measurements for Love and Rayleigh waves recorded on the USArray TA over a range of periods from 25 to 100 s. We estimate the arrival angle for each event at each station, and use this information to correct for off great circle arrival. We quantify the reduction in measurement uncertainty resulting from the use of the two-station method, as well as the effect of the arrival-angle corrections. The data set of phase measurements is inverted to obtain well-constrained models of the phase velocity structure of the Western United States. We compare these models with several published studies and with known geological structures. The Love and Rayleigh wave models are well suited for investigations of the 3-D velocity structure and radial anisotropy; we make the models available with this study to facilitate such future work.

2 METHODS

Two-station methods are an effective way to limit the sensitivity of a measurement to heterogeneity along the interstation path, cancelling effects of both the source and structure outside the array (e.g. Brisbourne & Stuart 1998). In this study, we implement a new two-station method that builds directly on single-station phase measurements, differencing single-station measurements for pairs of stations along the source–receiver great circle path. In addition, we make arrival-angle measurements for each single-station phase measurement and incorporate this additional information on ray geometry in our estimate of the interstation phase velocity.

This approach differs from traditional two-station methods (e.g. Satô 1955; Brune & Dorman 1963; Pilant & Knopoff 1964; Knopoff *et al.* 1966; Bloch & Hales 1968), in which the unknown system filter, representing earth's velocity structure between the two stations, is obtained by deconvolution of an input waveform recorded at one station from the output waveform recorded at a second station. Our approach takes advantage of modern methods for estimation of single-station phase delays (e.g. Trampert & Woodhouse 1995; Ekström *et al.* 1997), condensing the information in the waveforms at the two stations (the incoming and outgoing signals) to single-station phase measurements prior to interpreting the effect of the velocity structure (filter) between the two stations.

2.1 Single-station phase measurements

We make initial measurements of single-station phase delays using the method of Ekström *et al.* (1997). The observed surface wave signal u^S can be described by a phase, φ, and amplitude, A, as $u^S = A \exp[i\varphi]$. A trial fundamental-mode model seismogram, $u^M = A^M \exp[i\varphi^M]$, is calculated using the source and receiver locations, focal mechanism and predicted phase and amplitude effects of propagation in a long-wavelength 3-D earth model (SH8U4L8; Dziewonski & Woodward 1992). The deviation in phase between u^S and u^M is attributed to a perturbation to the propagation phase, $\varphi_P = \varphi_P^M + \delta\varphi = \frac{\omega X}{c^M + \overline{\delta c}}$, where c^M is the model phase velocity and $\overline{\delta c}$ is the average phase velocity perturbation over the distance X along the source–receiver path.

The unknowns A and $\overline{\delta c}$ are parametrized in terms of cubic B-spline polynomials. To solve for the corresponding coefficients, we first construct a whitening phase-matched filter using the model seismogram to suppress noise and amplify the fundamental mode surface wave signal, $W^M = \frac{1}{A^M} \exp[i\varphi^M]$. This filter is cross-correlated with the observed seismogram u^S in the frequency domain. The misfit between the resulting cross-correlation and the correlation of W^M with u^M is minimized to obtain the unknown coefficients. To avoid the common problem of cycle skipping when

Downloaded from http://gji.oxfordjournals.org/ at Columbia University on February 8, 2014

calculating the phase at short periods, we require that the surface wave dispersion curves vary smoothly with frequency and employ iterative frequency-band expansion, first using only longer periods, then gradually extending the passband to include shorter periods. Further details of the single-station method are given by Ekström *et al.* (1997).

2.2 Two-station phase measurements

We difference single-station phase delay measurements obtained at a pair of stations A and B lying nearly on the same source–receiver great circle path to obtain an average phase velocity attributable to the velocity structure between the two stations. The geometry of the system is shown in Figs 1 and 2. The distance between spherical wave fronts originating at the source and arriving at the two stations is denoted D_{AB} (Fig. 1a), and the interstation distance X_{AB}. We define an angle β between the interstation path and the great circle path from the source to receiver B. A surface wave may arrive at the pair of stations from an angle α off the great circle path (Figs 1b and 2), and in this case, the distance between spherical wave fronts arriving at the two stations will be the distance D'_{AB}. The angle between

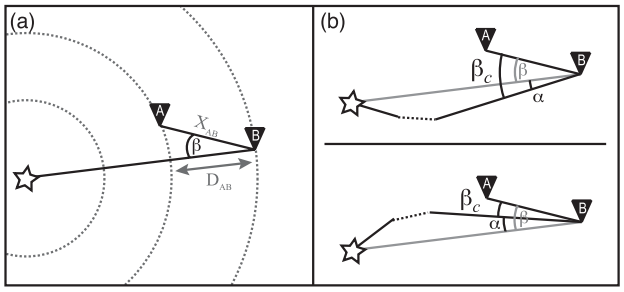

Figure 1. Source–receiver geometry for the two-station measurement. (a) β is the angle between the interstation path and the source-to-station-B great circle path. The distance used to calculate the interstation propagation phase is D_{AB}, the distance between spherical wave fronts intersecting the two stations. (b) β_c is the angle between the interstation path and the estimated true arrival path, at an angle α from the source-to-station-B great circle path. β_c can be larger or smaller than β, as shown in the top right and bottom right panels, respectively.

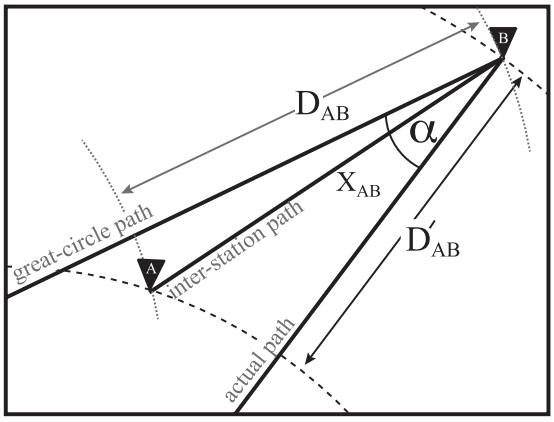

Figure 2. Station geometry for the two-station method, with the great circle path arrival azimuth and the actual arrival azimuth separated by the arrival angle α. D_{AB} is the distance travelled between stations along the great circle path. D'_{AB} is the distance travelled between stations along the actual arrival path.

the interstation path and the true, off great circle arrival path is denoted β_c.

When an arriving surface wave does not deviate from the great circle path, the average phase velocity c due to the velocity structure between the stations can be written

$$c(\omega) = \frac{\omega D_{AB}}{\frac{\omega D_{AB}}{c_0} + (\delta\varphi_B - \delta\varphi_A)}, \quad (1)$$

where ω is angular frequency, c_0 is the reference phase velocity at that frequency given by the Preliminary Reference Earth Model (PREM; Dziewonski & Anderson 1981) and $\delta\varphi_i$ is the phase anomaly measured at each station, calculated by subtracting the PREM reference phase φ_i^0 for station i from the observed phase at station i, or $\varphi_i - \varphi_i^0$.

When a wave arrives at a pair of stations at an angle other than that of the great circle path, the actual distance travelled from the closer station to the farther station, D'_{AB}, is not equal to the interstation distance X_{AB} or to the difference in distance between stations along great circle paths, D_{AB} (Fig. 2). Previous studies have noted that the interstation distance X_{AB} is always longer than D'_{AB}, resulting in a two-station measurement bias towards higher phase velocities (e.g. Yao *et al.* 2006). However, in comparison with the great circle distance D_{AB}, which may be offset from the interstation path by the angle β, the distance D'_{AB} may be shorter or longer. Two-station measurements that account for these geometric variations will not necessarily be biased towards higher phase velocities, and two-station measurements corrected for arrival angle α will not always be lower in phase velocity than their uncorrected counterparts.

With an estimate of the distance D'_{AB}, which we obtain as described in Section 2.3, eq. (1) becomes

$$c'(\omega) = \frac{\omega D'_{AB}}{\frac{\omega D_{AB}}{c_0} + (\delta\varphi_B - \delta\varphi_A)}. \quad (2)$$

The propagation phase φ_{AB} attributed to the interstation path, X_{AB}, is then calculated as:

$$\varphi_{AB}(\omega) = \frac{\omega X_{AB}}{c'(\omega)}. \quad (3)$$

2.3 Arrival-angle estimates

We wish to estimate the arrival angle α (Figs 1b and 2), and hence the distance D'_{AB}, to improve the accuracy of our description of the two-station geometry, as described above. Owing to the even and dense spatial coverage of the TA, we are able to use the single-station phase delay data set to estimate the geometry of the wave front and the direction of propagation of the wave near each station. We do this using data from a small subset, or 'mini array', of stations surrounding each station of interest. Measurements of particle motion polarization across a small region have indicated that wavefields for surface waves in the period range 16–100 s are generally coherent (Tanimoto & Prindle 2007), justifying the use of a plane wave approximation to measure the arrival angle.

Using the superscript 'a' to identify quantities related to the location of interest, we estimate α^a at a station r^a at a specified period using a mini array of N receivers, denoted r_i (Fig. 3). We select all stations within a radius R of r^a having single-station phase measurements for a given earthquake. We vary the apparent source location along an arc, keeping the epicentral distance L_0^a from r^a fixed. This effectively varies the arrival angle at station r^a. For each trial source location S_j^a, we consider the observed difference in phase between each station r_i and station r^a to be due to the difference in

Downloaded from http://gji.oxfordjournals.org/ at Columbia University on Februar

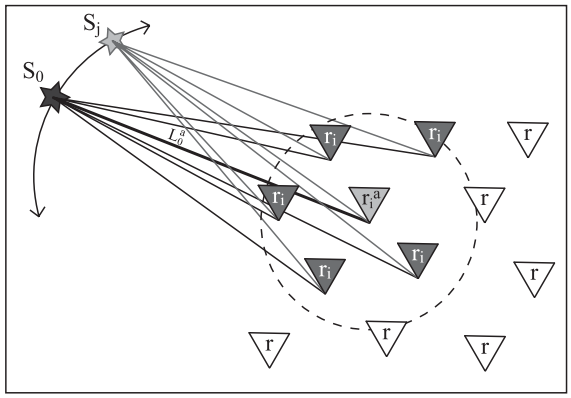

Figure 3. Illustration of search algorithm to find the best-fit apparent source location (S_*^a) for a given station (r^a) and source (S_0), using stations r_i that fall within a specified radius of r^a. The distance between S_0 and r^a, L_0^a, remains fixed for candidate source locations S_j.

epicentral distance divided by a local phase velocity c_j^a, such that $\delta\varphi_i = \varphi_i - \varphi^a = \omega\delta L_{ji}/c_j^a + C_j$. Here, δL_{ji} is the epicentral distance for an apparent source location S_j^a and receiver r_i differenced with the epicentral distance for r^a, L_0^a. The constant C_j accounts for errors in the observed phase at the reference station.

We solve for the local phase velocity c_j^a in a least-squares sense. The misfit between the predicted and observed phase associated with each trial source location S_j^a and the corresponding best-fit local phase velocity c_j^a is:

$$\Phi_j^2 = \sum_{i=1}^{N}\left[\delta\varphi_i - \left(C_j + \frac{\omega\delta L_{ji}}{c_j^a}\right)\right]^2. \quad (4)$$

We minimize this misfit for trial source locations corresponding to 0.5° steps in arrival angle, and select the location with the smallest misfit as the preferred apparent source location S_*^a, from which we calculate the arrival angle α_*^a at station r^a. The preferred local phase velocity c_*^a is also determined by the selection of S_*^a. We repeat this process for all stations and events meeting a set of basic quality criteria.

The arrival-angle estimation procedure thus yields an estimate of arrival angle for each station for each earthquake. The two-station phase velocity calculation described in eq. (2) requires a single arrival-angle estimate for each station pair, and we calculate this angle using the midpoint of the two best-fit apparent source locations. The local phase velocity measurements c_*^a, though incidental, provide independent measurements of phase velocity in the study area, and will be discussed in Section 4.1.

2.4 Inversion

For the determination of phase velocity maps, we parametrize the area of the Western United States using a 0.5° × 0.5° pixel grid. To model the two-station phase data, we use a ray theoretical framework with zero-width rays, thereby assuming each measurement is sensitive only to the interstation path. The benefits and limitations of this approach are discussed in Section 4.4. We calculate the predicted phase for each path k as

$$\varphi_k^{\text{pred}} = \sum_{i=1}^{N}\omega A_{ki}\, p_i, \quad (5)$$

where A contains the length of each segment of the interstation path crossing each pixel i, and p_i is the phase slowness for each pixel.

We invert for the model coefficients p_i using a Cholesky inversion technique. We regularize the inversion by minimization of the model roughness, given by:

$$R^2 = \sum_{i=1}^{N}\left[\sum_{j=N,S,E,W}\left(\frac{p_i - p_j}{d_{ij}}\right)^2\right], \quad (6)$$

where the index j refers to the pixel north, south, east and west of the ith pixel, and d_{ij} is the distance between pixel centres, corrected for changes in pixel size with latitude. The misfit between model and data is given by:

$$\chi^2 = \sum_k \frac{w_k^2}{\sigma^2}\left(\varphi_k^{\text{obs}} - \varphi_k^{\text{pred}}\right)^2, \quad (7)$$

where w is the weight for a path with n measurements. We choose w_k to be $w_k = 1 + \log_{10} n_k$. The weight factor is included to allow better-sampled paths to influence the resulting model more than paths with a small number of observations. We choose to use a constant data uncertainty, σ, for each period, as described in Section 3.5. The quantity to be minimized in the inversion is then

$$\chi^2 + \gamma R^2, \quad (8)$$

where γ is a scalar damping parameter.

3 DATA AND ANALYSIS

We analyse data recorded on the USArray TA from 2006 January to 2010 December. The size of our study area corresponds to the TA coverage through 2010 December, and thus extends from the West Coast of the United States to approximately 93°W longitude, between the southern and northern borders of the conterminous U.S. We use teleseismic earthquakes in the TA data set larger than magnitude 5.5, with focal depths shallower than 50 km, and epicentral distances in the range 10°–165°. Surface wave measurements are made at 11 discrete periods between 25 and 100 s. Rayleigh waves are measured on the vertical component and Love waves on the transverse component.

3.1 Single-station phase measurements

Single-station phase measurements are calculated for more than 1600 events (Table 1). The quality of each measurement is determined based on fit criteria using the same rules as in Ekström *et al.* (1997), and is denoted by A (high quality), B (good quality) or C (acceptable quality). For this study, we consider only A-quality measurements at all periods. It is more difficult to obtain high-quality measurements at short periods, due to increased sensitivity to more heterogeneous shallow structure and the large variations in phase that follow. This results in fewer A-quality data for short-period Love and Rayleigh waves. In addition, larger uncertainties in Love wave measurements are expected because of higher noise levels on the horizontal components. This greatly reduces the amount of A-quality data for Love waves at periods shorter than 50 s. We experimented with including B-quality measurements to expand the Love wave data set, but found that this led to an undesirable level of inconsistency in the phase measurements. Instead, we use the more limited data set of A-quality measurements, as for the Rayleigh waves. The number of data collected at each step of the method for each wave type is detailed in Table 1 for selected periods.

Downloaded from http://gji.oxfordjournals.org/ at Columbia University on February 8, 2014

Table 1. Available data.

Wave type	Period (s)	Events	Stations	One-station measurements	Two-station measurements Baseline	Two-station measurements Corrected	Interstation paths Baseline	Interstation paths Corrected	Paths in pref. model
Love qual. A	25	411	1056	5439	14 085	5240	12 026	4734	3892
	35	730	1101	11 585	26 509	14 848	22 873	13 317	7374
	50	1241	1135	42 758	171 021	115 534	111 735	80 797	32 691
	100	1241	1135	42 758	171 021	128 730	111 697	89 540	32 819
Rayleigh qual. A	25	1096	1158	100 817	682 976	391 010	222 750	155 928	56 558
	35	1375	1158	160 206	1 212 066	769 515	302 741	237 735	78 735
	50	1642	1159	272 033	2 205 538	1 418 955	364 076	288 277	92 725
	100	1642	1159	272 033	2 205 538	1 498 967	364 235	296 333	94 090

Notes: Summary of the number of measurements available at each step of the analysis, including total numbers of events and stations, single-station phase measurements, two-station phase measurements with no arrival-angle corrections (baseline) and with arrival-angle corrections (corrected) and unique interstation paths for both the baseline and corrected data sets. Numbers shown include all interstation path lengths greater than 100 km, with $\beta \leq 5^\circ$ and misfits within the prescribed range for arrival-angle estimates. Final column shows the number of unique interstation paths used to construct the preferred models, which includes path lengths between 350 and 750 km from the baseline data set for Love waves and the corrected data set for Rayleigh waves.

3.2 Baseline two-station phase measurements

We calculate initial two-station phase measurements for this data set without applying arrival-angle corrections. This results in our baseline data set. An initial data selection is made using β, the difference in backazimuth between the interstation path and great circle path between the event and farther station (Fig. 1a), and the interstation path length X_{AB}. The maximum value allowed for β, $\beta_{\max}$, was determined after consideration of the variance in phase for measurements obtained on single interstation paths. Previous studies have noted that allowing $\beta_{\max}$ larger than a few degrees results in greater scatter in the resulting phase measurements (e.g. Prindle & Tanimoto 2006). However, when we account for the geometry of the two stations by using D_{AB} in eq. (2), we do not observe a large increase in variance, at least up to $\beta_{\max} = 5^\circ$. Instead, we find that increasing $\beta_{\max}$ reduces uncertainty of the median phase for each interstation path by increasing the size of the data set. We choose $\beta \leq 5^\circ$ and initially set $X_{AB} > 100$ km, as we expect measurement error to be larger relative to the total phase for the shortest interstation paths.

The baseline data set contains a small number of outlying measurements. We exclude these by, at each period, calculating the average phase velocity from all measurements and then removing the 1 per cent of measurements that deviate the most from this average. The resulting data set has up to 2.2 million two-station phase measurements at a single period (Table 1). Some interstation paths align for several events, resulting in multiple phase measurements for a given path. For most paths, these repeat measurements are highly consistent, while for a small number of paths, the measurements span a wide range of phase values. This scatter may be caused by many factors, including multipathing, overtone interference and finite-frequency propagation effects. These factors are explored more in Section 4.4; here, we select the median value for each interstation path to reduce the influence of outliers.

3.3 Arrival-angle estimates

We estimate the best-fit local phase velocity and arrival angle at all stations with at least three single-station phase measurements within a 1°-radius mini array for Rayleigh waves and a 2°-radius mini array for Love waves. These criteria were chosen with the goal of producing robust arrival-angle measurements, balancing the considerations that, for a single event, smaller radii can resolve shorter wavelength variations in arrival angles and phase velocity anomalies, while larger radii smooth both the effect of structure and noise in the measurements. Similarly, requiring more stations within a given radius provides better constraints on the arrival angle and local phase velocity but limits the measurements to only the best-covered areas. Measurements with best-fitting arrival angles larger than $\pm 15^\circ$ are discarded. Although some larger arrival-angle measurements may be real, particularly close to the ocean–continent boundary (Tanimoto & Prindle 2007), some may be spurious, or may represent local complexities in the wavefield that are beyond the scope of this study. This selection results in a small loss of data, with 97 per cent of the measurements being retained. We wish to use only good estimates of arrival angle and corresponding local phase velocity, which we define in terms of the misfit between the observed and predicted phase at all stations in the mini array. Although large misfits are not always associated with local phase velocities outside the expected range, or vice versa, we set a maximum allowed misfit for each wave type, scaled by the frequency. This results in 91 per cent of the remaining data being retained for Love waves and 98 per cent for Rayleigh waves.

Individual estimates of local phase velocity are highly variable for different earthquakes, and can be outside the range of expected values (Fig. 4). However, after averaging estimates at a given station for many events, noise and any remaining source effects are largely suppressed. The resulting maps show smooth spatial variations in velocity, and velocity anomalies with convincing size, strength and location (Fig. 5).

3.4 Corrected two-station phase measurements

Using the arrival-angle estimates derived in the previous section, we calculate corrected two-station phase measurements for interstation distances greater than 100 km. As for the uncorrected two-station measurements, we require β_c, the angle between the interstation path and the backazimuth corresponding to the average arrival angle for the station pair (see Fig. 1b), to be less than or equal to 5°, and the 1 per cent of the data that lies farthest from the average corrected two-station phase velocity is discarded to remove outliers.

The arrival angle used to make the phase correction corresponds to the midpoint between apparent source locations for the two stations. In some instances, the apparent source locations, and corresponding arrival angles, are nearly equivalent for the two stations,

Downloaded from http://gji.oxfordjournals.org/ at Columbia University on Februar

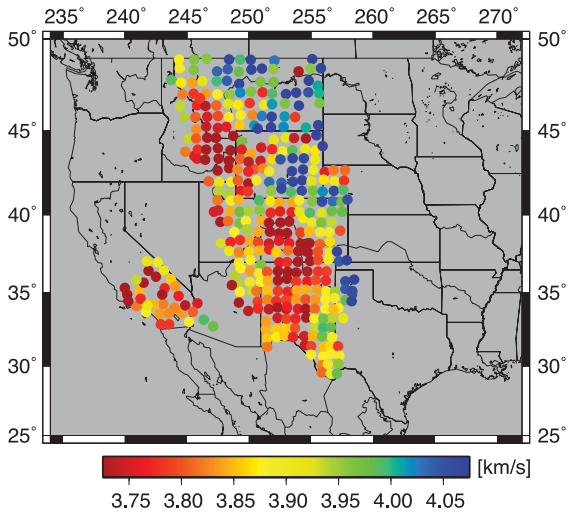

Figure 4. Local best-fit phase velocity results for 50-s Rayleigh waves for a single event located in Tonga. Measurements were made using a mini array with 1° radius.

consistent with the energy propagating along a simple path and most refraction occurring outside the array. In other cases, the apparent source locations and arrival angles at the two stations are different, suggesting that refraction has taken place near the interstation path. Examining two interstation paths with many measurements (Fig. 6a), we find that, for the shorter inter-station distance, the difference in arrival angle for a single event at the two stations usually is small, with most values less than 3°. For the longer interstation path, the difference in arrival angle is typically larger, shown by the wider distribution of values. This is partially explained by geometrical differences in the two stations' orientations with respect to the source, but is also compatible with the notion that waves travelling longer interstation paths are more likely to encounter velocity gradients, resulting in larger arrival-angle variations for the station pair. This observed pattern is representative of the full data set, as illustrated in Fig. 6b. We choose to reduce our data set by selecting the median value of the two-station phase estimates for each interstation path with multiple measurements.

3.5 Data uncertainties

An advantage of two-station methods over one-station methods is that several sources of uncertainty in the phase measurement are cancelled. One-station measurements depend on the accuracy of the source location and focal mechanism, and phase anomalies reflect variations from the entire source-station path. Two-station measurements do not depend on these factors, and so the final datum should have a smaller associated uncertainty.

For each period and wave type for both our baseline and corrected data sets, we calculate the data uncertainty parameter σ using the variations in observed phase on a given interstation path with multiple measurements. We compute the difference in phase between all two-station phase measurements on that single path. These phase differences are compiled for all interstation paths with multiple

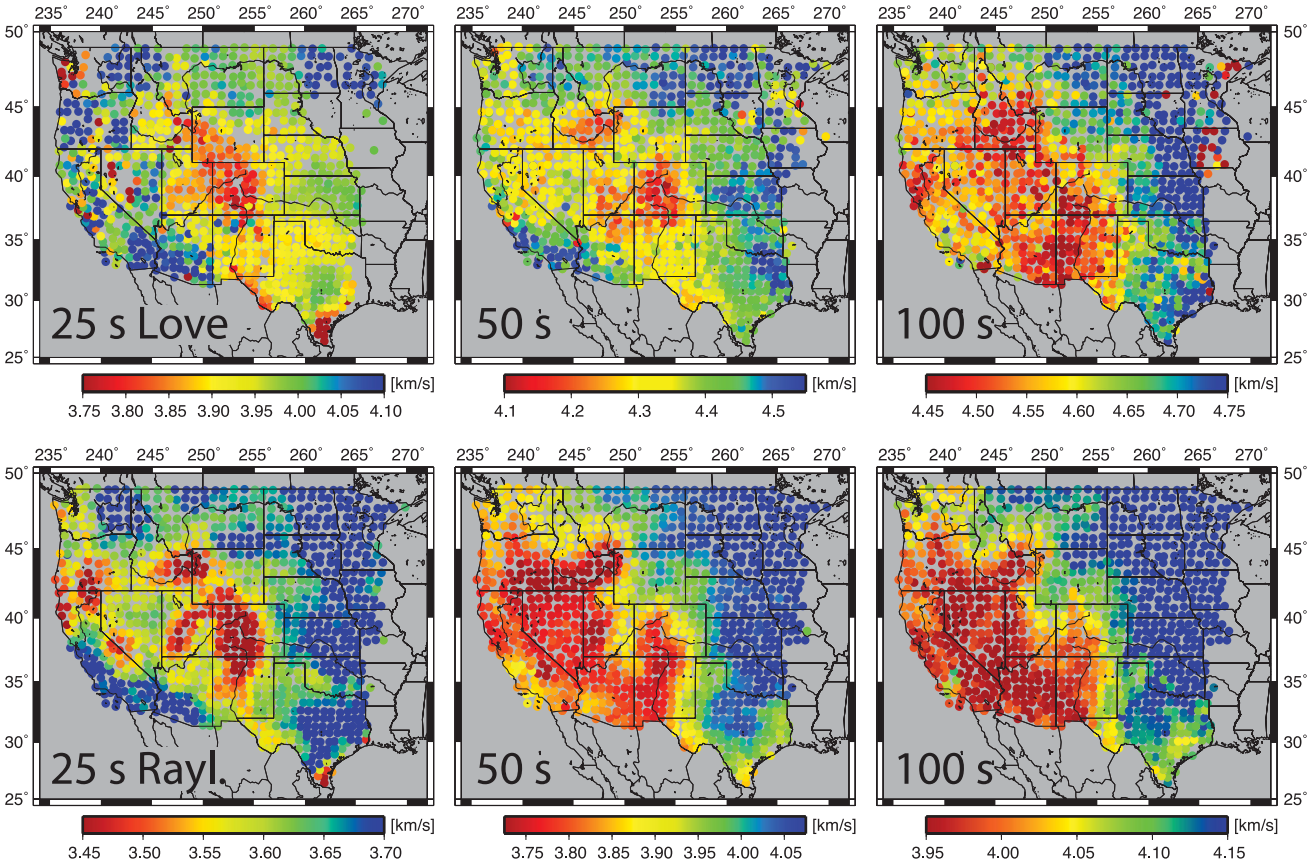

Figure 5. Median local phase velocity estimates at each station location for Love waves (top) and Rayleigh waves (bottom) at 25-, 50- and 100-s period. Symbol at each station represents the median value for all estimates meeting the misfit criteria.

Downloaded from http://gji.oxfordjournals.org/ at Columbia University on February 8, 2014

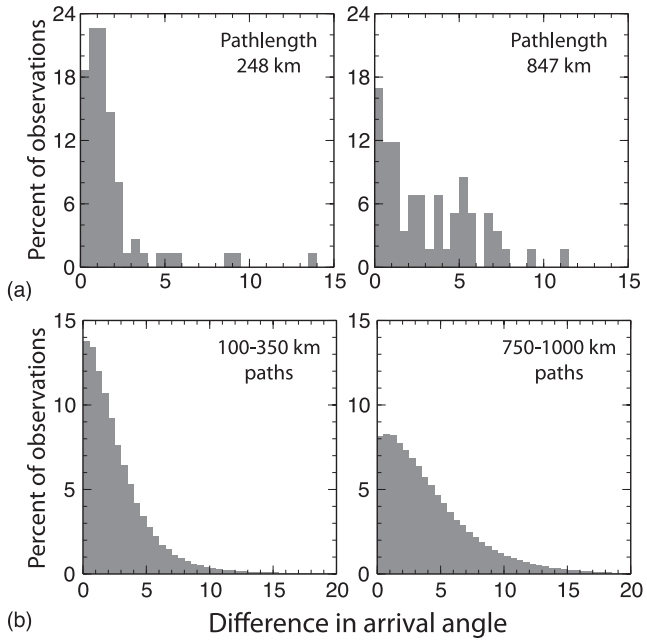

Figure 6. Difference in estimated arrival angle at two stations recording the same earthquake and satisfying the criteria for the two-station phase measurements. Arrival-angle measurements were made on 50-s Rayleigh waves, using a 1° mini array. All figures are bar graphs folded about zero, shown as per cent of the available data. (a) Top left shows results for a single, shorter (248 km) interstation path with measurements from 68 different events. Top right shows results for a single, longer (847 km) interstation path, with measurements from 54 events. (b) Bottom graphs show results for all interstation path lengths between 100 and 350 km (left) and 750 and 1000 km (right).

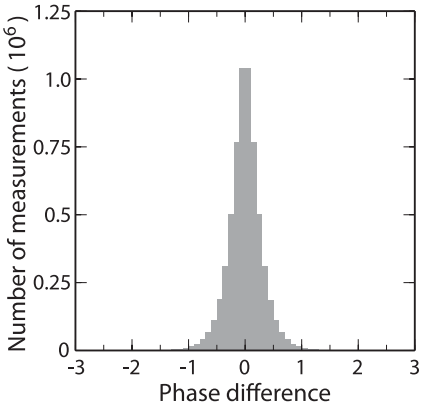

Figure 7. Distribution of the differences in phase between multiple two-station phase measurements from the same interstation path, for 50-s Rayleigh waves. Number of measurements shown in millions. The standard deviation of this distribution is two times the standard deviation of the distribution of errors in two-station phase measurements.

observations, resulting in a distribution with a mean of zero (Fig. 7). For uncorrelated errors, this distribution of phase differences is expected to have a standard deviation of two times the uncertainty in a single two-station phase measurement, or 2σ (e.g. Ekström *et al.* 1997). Calculated values of σ are listed in Table 2. As noted by Ekström *et al.* (1997), this estimate excludes the uncertainty resulting from systematic errors, and hence should be considered a minimum estimate.

The two-station uncertainty estimates can be compared with those made by Ekström (2011) for single-station phase measurements at the same periods. As expected, the two-station measurements show lower uncertainty at all periods (Table 2). For Rayleigh waves, the uncertainty for two-station measurements is smaller by a factor of 4–8 at all periods. The uncertainties are also smaller for Love waves, though the differences are not as large: the two-station measurements have uncertainties smaller by only a factor of 2 or less at most periods, with the greatest reduction at the shortest periods. The differences in the reduction in uncertainty between Love and Rayleigh waves may indicate an important difference in the propagation behaviour between the two wave types, which in turn affects the degree to which the two-station method can be successful. One possible factor may be overtone interference; though overtone contamination is found to be small for single-station measurements made using the Ekström *et al.* (1997) approach (Nettles & Dziewoński 2011), it may be large relative to the phase accrued along the shorter paths used in a two-station method. This effect is discussed further in Section 4.4. Here, we conclude that the two-station method improves upon the single-station method for regional studies.

A comparison between the uncertainties calculated for our baseline and corrected two-station measurements shows smaller uncertainties for the corrected data set at all periods. At shorter periods, the corrected uncertainty is smaller by a factor of ∼2, while at long periods the corrected uncertainty is smaller by a factor of 1.1–1.5. This reduction in uncertainty is likely due in part to improvements from the corrected two-station method, and in part to the selection of a smaller, high-quality data set, which is a result of making the mini array estimates. The improvements from the method will be explored further in Section 4.2.

3.6 Inversion

We invert the baseline and corrected two-station phase data sets separately in order to determine which method gives better results. After performing trial inversions using the full data set as well as different subsets of the data, we choose to limit the interstation path length such that 350 km $\leq X_{AB} \leq$ 750 km. This equates to roughly one-third of the full data set (Table 1). We choose to remove the longer paths to improve the short-wavelength resolution in our final models, and because longer paths increase the possibility that the wave front will fail to behave as a plane wave and distort the two-station measurements. We exclude shorter paths because the measurement errors in phase are larger relative to the propagation phase, translating to greater uncertainty in phase velocity than for longer paths. In our inversions, we use the data uncertainties calculated for the full data set, as given in Table 2. The value of the damping parameter γ is chosen subjectively at each period, with smoothness being favoured over higher variance reduction. The same damping parameter is used for inversion of the baseline and corrected data sets at each period.

This analysis leads to two separate phase velocity models at each period: the baseline model and the arrival-angle-corrected model. The variance reduction for all models is given in Table 3 with respect to a model consisting of the mean-retrieved phase velocity at each period. The variance reduction for Love waves is low at longer periods, reflecting variability in the data that cannot be fit by the model. The variance reduction for Rayleigh waves is high at all periods, ranging from 77 to 92 per cent. A measure of the goodness-of-fit, χ^2/N_{wt}, is also given in the table, calculated from:

$$\chi^2 = \sum_{i=1}^{N} \frac{w_i^2}{\sigma_i^2} \left(\varphi_i - \varphi_i^P\right)^2, \quad \text{and} \quad N_{wt} = \sum_{i=1}^{N} w_i^2. \tag{9}$$

Downloaded from http://gji.oxfordjournals.org/ at Columbia University on Februar

Table 2. Phase measurement uncertainties.

Period (s)	Love			Rayleigh		
	One-station (A)	Two-station		One-station (A)	Two-station	
		Baseline	Corrected		Baseline	Corrected
25	0.903	0.158	0.078	0.951	0.306	0.132
27	0.757	0.142	0.084	0.833	0.237	0.120
30	0.589	0.132	0.061	0.709	0.179	0.098
32	0.595	0.295	0.153	0.759	0.245	0.133
35	0.477	0.256	0.184	0.648	0.185	0.109
40	0.385	0.213	0.137	0.533	0.144	0.092
45	0.338	0.182	0.123	0.454	0.124	0.084
50	0.403	0.278	0.239	0.569	0.180	0.106
60	0.319	0.231	0.203	0.437	0.135	0.090
75	0.262	0.214	0.198	0.331	0.094	0.070
100	0.215	0.148	0.139	0.250	0.067	0.057

Notes: Estimated uncertainties for single- and two-station phase measurements, based on $\frac{1}{2}$ the standard deviation of the distribution of phase differences for multiple measurements on the same path (two-station) or similar paths (one-station). Two-station measurement uncertainty reflects quality A data with no arrival-angle corrections (baseline) or with arrival-angle corrections (corrected). Two-station uncertainties are calculated using all path lengths greater than 100 km. A sample distribution is shown for two-station phase measurements of 50-s period Rayleigh waves in Fig. 7. Single-station phase uncertainties are from Ekström (2011).

Table 3. Model fits to data.

Period (s)	Love				Rayleigh			
	Variance reduction		Goodness-of-fit		Variance reduction		Goodness-of-fit	
	Baseline	Corrected	Baseline	Corrected	Baseline	Corrected	Baseline	Corrected
25	80.92	90.53	2.78	4.70	76.56	86.87	1.76	4.69
27	77.34	88.57	3.79	4.47	79.66	87.73	2.12	4.67
30	79.24	87.72	3.70	9.32	83.50	89.37	2.38	5.08
32	50.26	52.93	2.47	8.06	82.54	88.00	1.34	3.09
35	52.10	53.30	2.52	4.06	86.64	90.60	1.58	3.23
40	50.45	51.83	3.24	6.50	88.95	91.91	1.88	3.39
45	45.88	47.38	4.75	9.40	89.84	92.14	2.02	3.40
50	26.95	27.06	3.63	4.61	87.80	91.63	1.05	2.03
60	25.27	25.76	4.09	5.09	88.26	91.22	1.17	1.97
75	20.75	21.02	4.31	5.03	88.31	90.90	1.27	1.76
100	22.95	22.90	4.05	4.54	84.86	86.57	1.15	1.37

Notes: Variance reduction with respect to a weighted mean model achieved by inversion of the baseline and corrected data sets for Love and Rayleigh waves at each period. Goodness-of-fit, calculated as the total variance divided by the weighted number of measurements or χ^2/N_{wt}, is also shown.

The goodness-of-fit achieved ranges from 1.05 to 9.40, with values closer to 1 being more desirable. We discuss and select our preferred models in the following section.

4 PREFERRED MODELS

4.1 Comparison with local phase velocity models

We have measured local phase velocities in the process of making mini array arrival-angle estimates, and averaged them over many events to generate local phase velocity estimates at most stations (Fig. 5; Section 3.3). These local measurements are based on the phase information in multiple very short interstation paths within each mini array. They are, therefore, independent of the models that result from inversion of our two-station measurements, which all derive from paths longer than 350 km. We compare the two results to assist in our assessment of the maps derived from the two-station measurements.

Local phase velocity estimates are very consistent with the phase velocity models from inversion of baseline two-station measurements for Rayleigh waves. Evaluating the models at each station location where we have a median local phase velocity estimate, we find correlation values of 91–97 per cent. Furthermore, scatter plots of Rayleigh wave measurements from the two methods fall near a 1:1 line (Fig. 8), suggesting there is no bias in the mini array method and independently confirming our inversion results. The good agreement between the two sets of results also increases our confidence in the Rayleigh wave arrival-angle estimates from the mini array approach.

Love wave estimates from the two methods are much less consistent, with correlation values of 32–72 per cent. Love wave scatter plots at periods of 35 s and longer also show an offset of the mini

Downloaded from http://gji.oxfordjournals.org/ at Columbia University on February 8, 2014

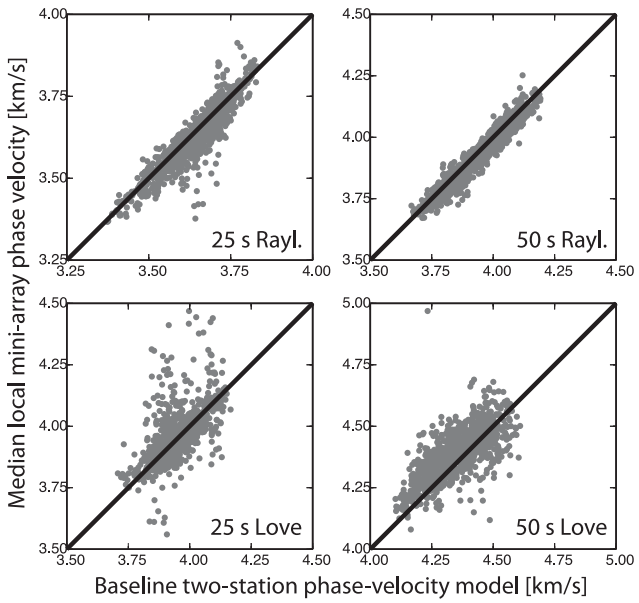

Figure 8. Scatter plots showing the phase velocity for the baseline two-station model evaluated at each station location versus the estimated local median phase velocity at each station for Rayleigh waves (top) and Love waves (bottom) at 25- and 50-s period. Black line shows 1:1 relation.

array measurements to higher phase velocities compared with the baseline two-station phase velocity model (Fig. 8). This offset may be due to overtone interference (Section 4.4), or a geometrical effect of the mini array method. It is possible that the corresponding Love wave arrival-angle estimates are also affected. We, therefore, choose not to use the Love wave arrival-angle estimates in this study, and identify the discrepancy between the two types of results as a topic for future study. Here, we select the phase velocity maps from the baseline data set to be our preferred model for Love waves.

4.2 Improvements from arrival-angle corrections

To investigate the extent to which arrival-angle corrections improve the two-station phase velocity measurements for Rayleigh waves, we compare the variance reduction achieved by phase velocity models derived from the corrected phase measurements with models derived from baseline uncorrected phase measurements (Table 3). At all periods, models made with corrected data produce greater variance reduction. This indicates that the corrected two-station phase measurements are more self-consistent throughout the study region than the uncorrected measurements. Values for the goodness-of-fit (χ^2/N_{wt}) for the corrected model are generally higher than for the baseline model, because the uncertainty for the corrected data set is lower. If we remove the effect of the measurement uncertainty from the goodness-of-fit (eq. 9), we find that the observed goodness-of-fit from the corrected models is 1.2–1.8 times better than that from the baseline model.

We also compare the phase measured using waves travelling in one direction on an interstation path versus measurements made using waves travelling the opposite direction on the same path. We use the median for all measurements travelling in one direction, or from station A to station B, and compare this with the median phase for all measurements on the same path using waves travelling from station B to station A (Fig. 9a). Ideally, these reciprocal two-station measurements would have no directional dependence, since

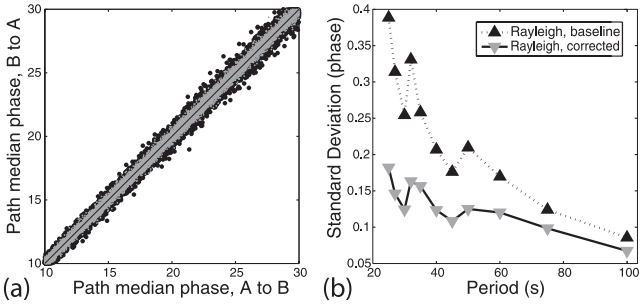

Figure 9. (a) Example of differences in median phase measurements for waves travelling in one direction, station A to station B, with the median phase measurement for waves travelling in the opposite direction, B to A, for 50-s Rayleigh waves for a single path. Black dots: uncorrected measurements; grey dots: corrected measurements. The scatter from the one-to-one line (black) is reduced by applying arrival-angle corrections to the measurements. (b) Plot of the standard deviation of the distribution of deviations from the one-to-one line, as in (a), for Rayleigh waves at all periods for the full data set. We assume a mean of zero. In all cases, corrections reduce the differences in reciprocal-path phase.

there are few physical causes of $1-\psi$ anisotropy for surface waves. Although reciprocal two-station measurements are well correlated overall, differences in directional median phase on reciprocal paths are common. This scatter likely results from several factors, including off great circle propagation. This inference is supported by the effect of arrival-angle corrections on the comparison: corrected two-station phase velocity measurements show notably less scatter than uncorrected measurements. We quantify this effect by comparing the distribution of deviations from the ideal one-to-one line for uncorrected and corrected phase measurements. The standard deviations of these distributions for each period and wave type show a reduction in the spread of deviations for the corrected data set (Fig. 9b).

Our experiments thus indicate that the arrival-angle correction improves the two-station measurement for Rayleigh waves. We select the maps derived from the corrected data as our preferred Rayleigh wave phase velocity model.

4.3 Phase-velocity maps

Because of the improvements in variance reduction and other quantitative measures, we have selected the phase velocity maps from the corrected data set as our preferred models for Rayleigh waves (Section 4.2). Based on the likely inconsistencies in the Love wave arrival-angle estimates, we have selected the baseline models as our preferred models for Love waves (Section 4.1).

The final models are shown in Figs 10 and 11 for 6 periods ranging from 25 to 100 s period. The phase velocity is given as a per cent variation with respect to the model mean. Rayleigh wave phase velocities range from 3.4 to 4.3 km s^{-1}, while Love wave phase velocities range from 3.7 to 4.9 km s^{-1}. The wavelength of anomalies varies with period for both wave types. At 25-s period, fast to slow variations occur over length scales of a few degrees, whereas at 100 s, variations occur smoothly over tens of degrees. At a given period, the pattern of anomalies is similar for Love and Rayleigh waves, but consistent with expected differences from the differing sensitivity kernels. The observed anomalies will be discussed further in Section 5.3.

Downloaded from http://gji.oxfordjournals.org/ at Columbia University on Februar

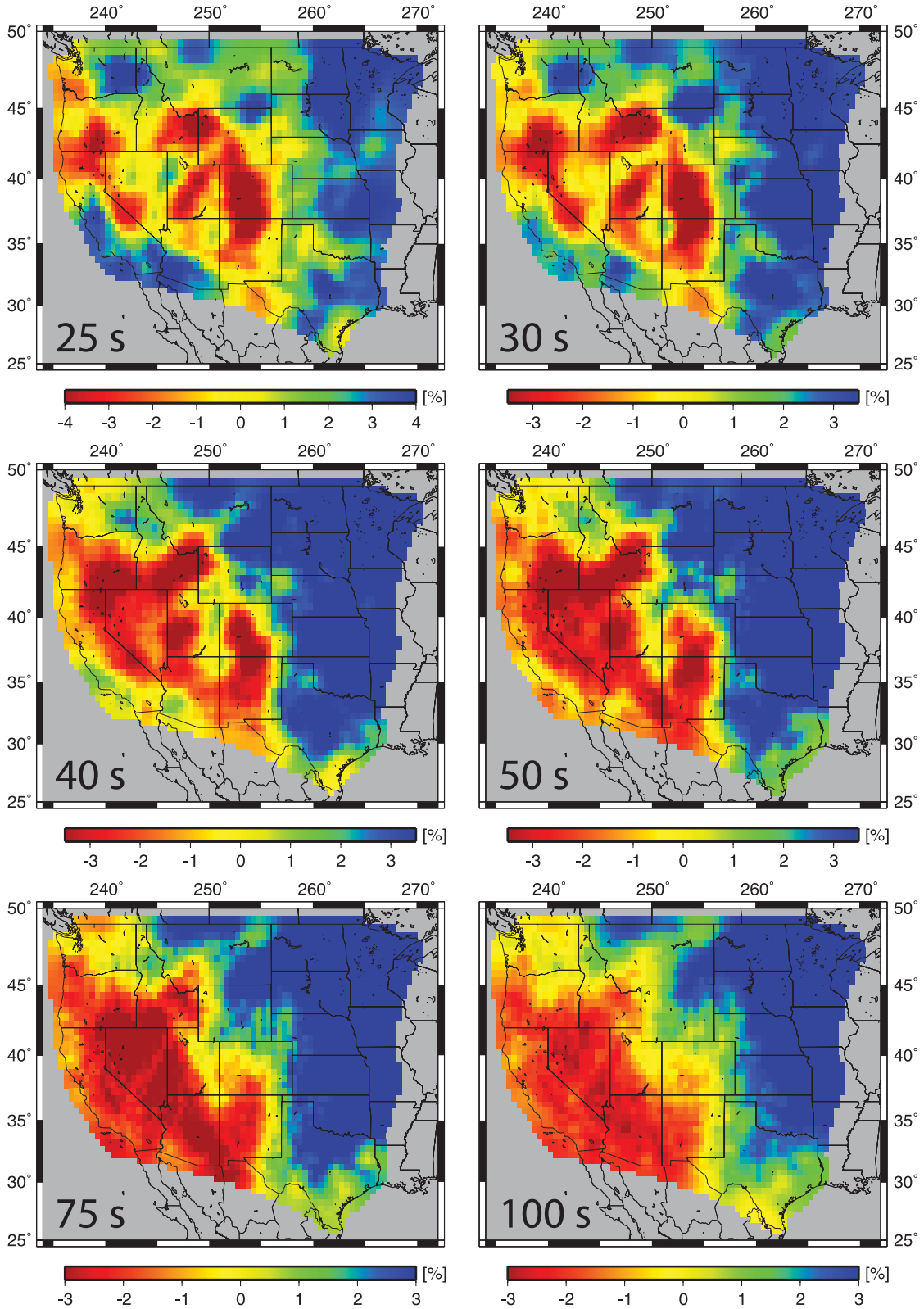

Figure 10. Rayleigh wave phase velocity models from two-station phase measurements corrected for arrival angle at 25-, 30-, 40-, 50-, 75- and 100-s period. The model includes the area with path coverage, expanded by one pixel in each direction. Values are given as a per cent deviation with respect to the model mean at each period.

Downloaded from http://gji.oxfordjournals.org/ at Columbia University on February 8, 2014

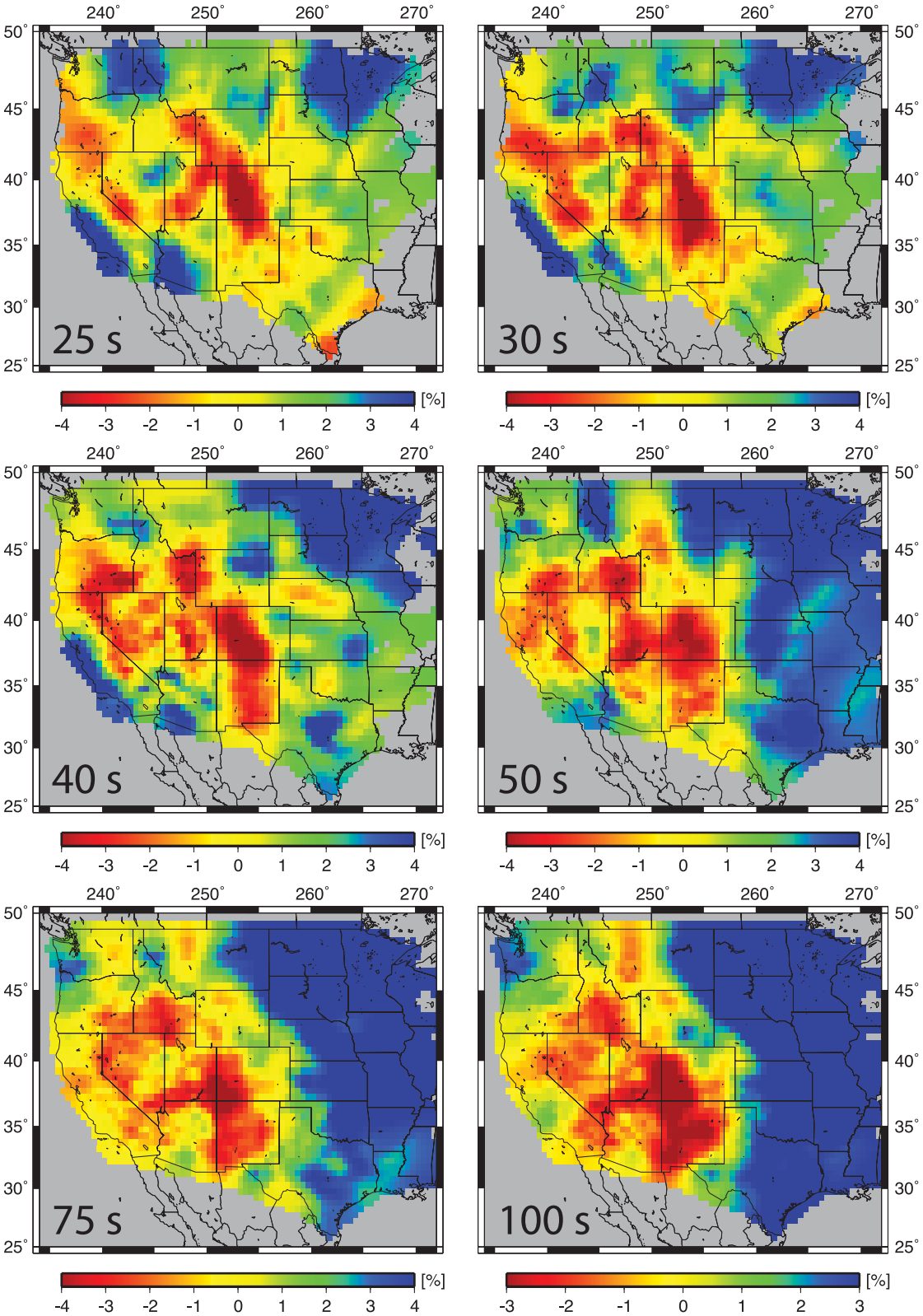

Figure 11. Love wave phase velocity models from two-station phase measurements at 25-, 30-, 40-, 50-, 75- and 100-s period. Baseline phase measurements were used. The model includes the area with path coverage, expanded by one pixel in each direction. Values are given as a per cent deviation with respect to the model mean at each period.

Downloaded from http://gji.oxfordjournals.org/ at Columbia University on Februar

4.4 Sources of error

4.4.1 Ray theory

Many commonly used methods for interpreting phase or traveltime measurements are based on ray theory, with the observation related to the intrinsic velocity by a ray path integral. Ray theory is exact in the limit of infinite frequency, and generally applicable when the length scale of the heterogeneity is greater than the seismic wavelength. When this is not the case, the sensitivity of the wave is not limited to the ray path, but rather includes a broader area surrounding it. The limitations of ray theory have been well documented (e.g. Woodhouse & Girnius 1982; Spetzler *et al.* 2002; Boschi *et al.* 2006). The alternative is to include finite-frequency effects, usually by defining a 2-D or 3-D sensitivity kernel (e.g. Meier *et al.* 1997; Yoshizawa & Kennett 2002, 2005; Zhou *et al.* 2004; Tromp *et al.* 2005; Peter *et al.* 2007; Lin & Ritzwoller 2010).

Comparisons of ray theoretical and finite-frequency approaches have shown that 3-D kernels can provide improvements in predicting fundamental mode surface wave traveltime anomalies and recovering small-scale heterogeneity (e.g. Zhou *et al.* 2005; Peter *et al.* 2009). However, accurate 3-D kernels are computationally expensive, and several authors have found that ray theory performs equally well or better than lesser approximations in situations with dense path coverage and with appropriate regularization (e.g. Spetzler *et al.* 2002; Sieminski 2004; Boschi *et al.* 2006; Trampert & Spetzler 2006). In light of this, and given the exceptional data coverage at most periods, we have confined the sensitivity to the ray path to simplify the calculations. A further simplification used here, common to two-station methods, involves the assignment of a phase velocity measured slightly off the interstation path to the interstation path in the inversion. These limitations are most likely to affect small-scale structure, and we expect our choice of damping to help mitigate such effects in the models we present here.

4.4.2 Plane wave assumption

A premise of many array-based measurements is that the wavefield can be approximated locally as a plane wave, even when the wave front is distorted on a larger scale moving through a heterogeneous earth. This is a commonly accepted assumption for teleseismic studies using arrays covering a small area. Even for such situations, however, Wielandt (1993) noted biases in phase measurements introduced by non-planar wavefield geometries.

The spatial variation in arrival angles we observe for a single event at many different stations is likely related to the effects of a non-planar wavefield. By correcting the two-station geometry using the arrival angles, we remove much, but probably not all, of the error resulting from such wavefield distortions. These errors are likely largest for a station pair with very different arrival angles, indicating scattering along the interstation path. At the shortest periods used in this study, the observed arrival angles increase in amplitude, suggesting that we may be approaching the limit of the plane wave assumption at these periods.

4.4.3 Overtones

Several authors have shown that overtones can affect the single-station phase measurement method, but with a sufficient distribution of sources and path lengths, the effect is not systematic (Boore 1969; Forsyth 1975; Nakanishi & Anderson 1983; Nettles & Dziewoński 2011). It is not well known how overtones might influence multiple-station methods such as the two-station and mini array methods used here, though some investigations have been made regarding short-period and active-source data (e.g. Forbriger 2003; Kimman *et al.* 2011). Due to the similar fundamental mode and overtone group velocities of Love waves, contamination of fundamental mode phase measurements is a more serious concern for this wave type (e.g. Nettles & Dziewoński 2011). We have already mentioned overtone contamination as a possible explanation for the smaller reduction in uncertainty for two-station phase measurements compared to single-station phase measurements for Love waves, and for the spuriously high local mini array phase velocity estimates for Love waves. By using the broad path distribution of the TA, a large and globally distributed number of earthquake sources, and not using the Love wave arrival-angle estimates, we believe that the phase velocity models presented here are not strongly affected by overtone interference.

4.4.4 Anisotropy

Surface wave azimuthal anisotropy has been observed in the Western United States, with average strengths of approximately 1–2 per cent in the period range we discuss here (e.g. Marone & Romanowicz 2007; Beghein *et al.* 2010). However, we expect the azimuthal averaging that is part of our inversion to reduce the effect of azimuthal anisotropy, particularly given the excellent azimuthal coverage afforded by the TA. The high correlation between the preferred models and the mini array results, which should be affected by anisotropy in different ways, suggests that the azimuthal averaging has the expected effect. This high correlation is especially indicative for Rayleigh waves, which normally show the strongest azimuthal signal.

5 DISCUSSION

5.1 Effect of arrival-angle corrections

In this study, we find that estimated arrival angles at each period span the allowed range from -15° to $+15^\circ$, with generally larger angles at shorter periods. Locally, the difference in estimated phase velocity resulting from corrections for arrival angle can be up to 4 per cent with respect to the model mean, although most values fall in the range 0–1 per cent. These differences are similar to previous observations: Alsina *et al.* (1993) used a wave front reconstruction method similar to our mini array method, and found that typical deviations for a wave travelling a largely oceanic path before crossing the European continental margin were no greater than $\sim 8^\circ$ at 15–100 s period, resulting in an error in interstation phase velocity of less than 1 per cent.

The change in the Rayleigh wave velocity models due to arrival-angle corrections is illustrated in Fig. 12, where the left column is the model derived from baseline (uncorrected) phase measurements, the middle column is the model derived from corrected phase measurements and the right column is the difference. The values shown indicate the change in velocity due to the arrival-angle corrections as a per cent of the mean velocity of the two models for each period: blue indicates the corrected model is faster than the baseline, while red indicates the corrected model is slower. At all periods, 70–75 per cent of the pixels show a change to slower velocities.

For Rayleigh waves at short periods (25 s), the changes to the velocity model resulting from the corrections are concentrated along the West Coast, where the ocean–continent transition crossed by all waves with sources in the southwest, west and north Pacific

Downloaded from http://gji.oxfordjournals.org/ at Columbia University on February 8, 2014

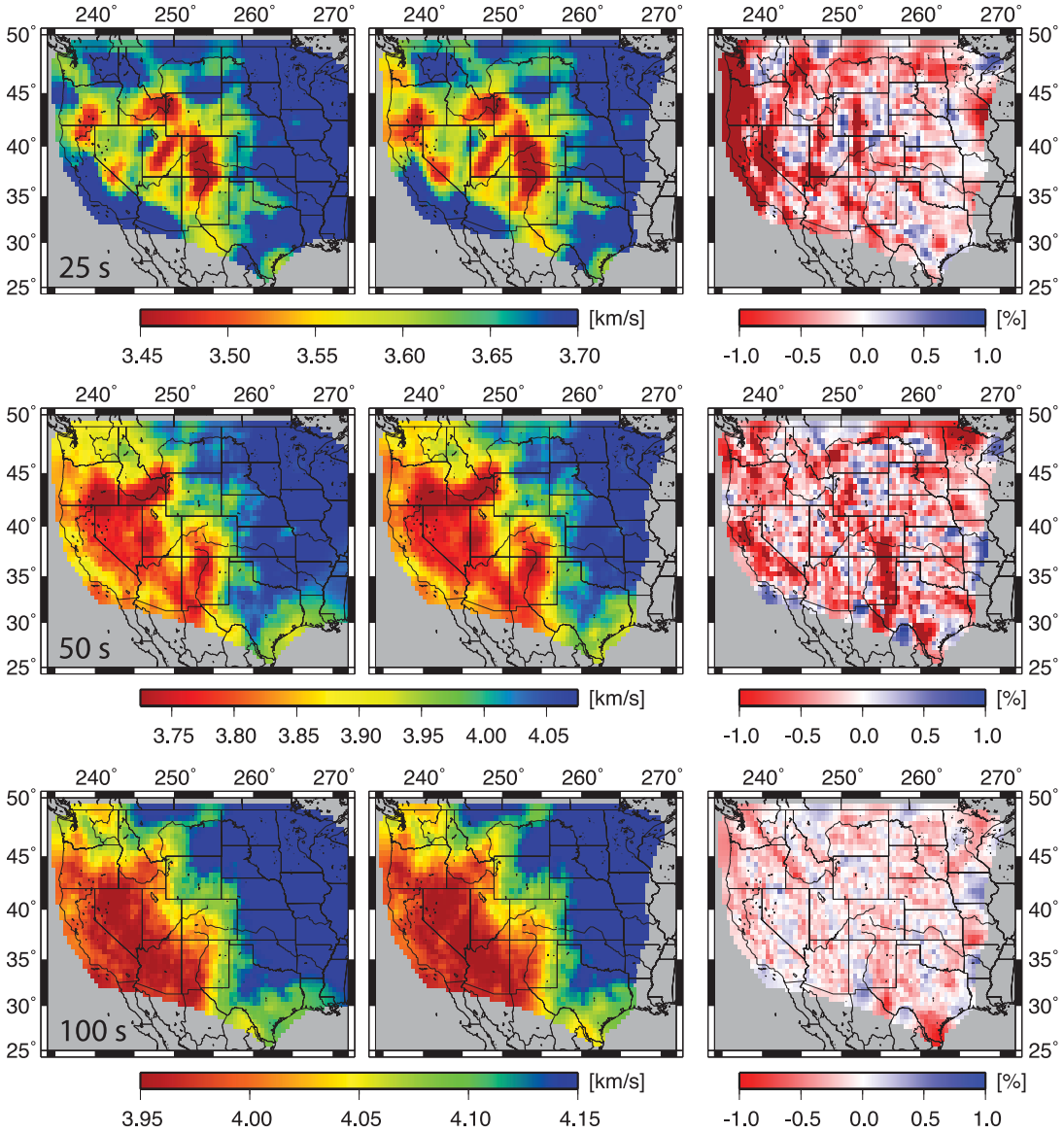

Figure 12. Rayleigh wave phase velocity models from baseline two-station phase measurements (left), and models from phase measurements corrected for arrival angle (middle) at 25-, 50- and 100-s period, top to bottom. Phase velocity values are shown in the area with path coverage, expanded by one pixel in each direction. Right column shows the difference between the two models (corrected minus baseline) as a per cent of the average velocity of the two models.

is expected to cause large deviations. For longer period Rayleigh wave models, 50–100 s, the changes in velocity are smaller and more diffusely distributed across the Western United States, likely reflecting the reduced sensitivity of these waves to the relatively large velocity variations in structure at shallower depths, and their larger sensitivity to greater depths, where velocity variations are expected to be weaker.

We expect that Love wave phase velocity models would be similarly affected by arrival-angle corrections. This would likely mean changes in velocity of several per cent, with larger changes at shorter periods and concentrated near the West Coast. As with the Rayleigh wave models, we would not expect arrival-angle corrections to affect the first-order features in the Love wave phase velocity maps.

5.2 Comparison with published models

Western North America has been well studied by seismic tomography, both in the context of global models and in higher resolution regional studies. We compare our phase velocity models with earlier results, to note features that are consistent across models and wavelengths, and those that provide new information. Here, we compare our study with results from three published models (Fig. 13).

The first comparison is with the combination of a global radially anisotropic mantle velocity model, S362ANI (Kustowski *et al.* 2008), and a global crustal model, CRUST 2.0 (Bassin *et al.* 2000). These models are often used together to predict velocities or seismograms when the effects of global 3-D structure are desired (e.g. Tromp *et al.* 2010). S362ANI was developed in a ray theoretical framework using teleseismic body-wave traveltimes, fundamental mode surface wave measurements and overtone data from waveform inversions. CRUST 2.0 was developed by compiling seismic data on crustal thickness, velocity and density, averaged globally for similar geological and tectonic settings. These measurements were combined with published ice and sediment thicknesses to create a collection of 1-D crustal profiles. Each $2^\circ \times 2^\circ$ grid cell is assigned one such profile, composed of ice, water, soft sediments, hard

Downloaded from http://gji.oxfordjournals.org/ at Columbia University on Februar

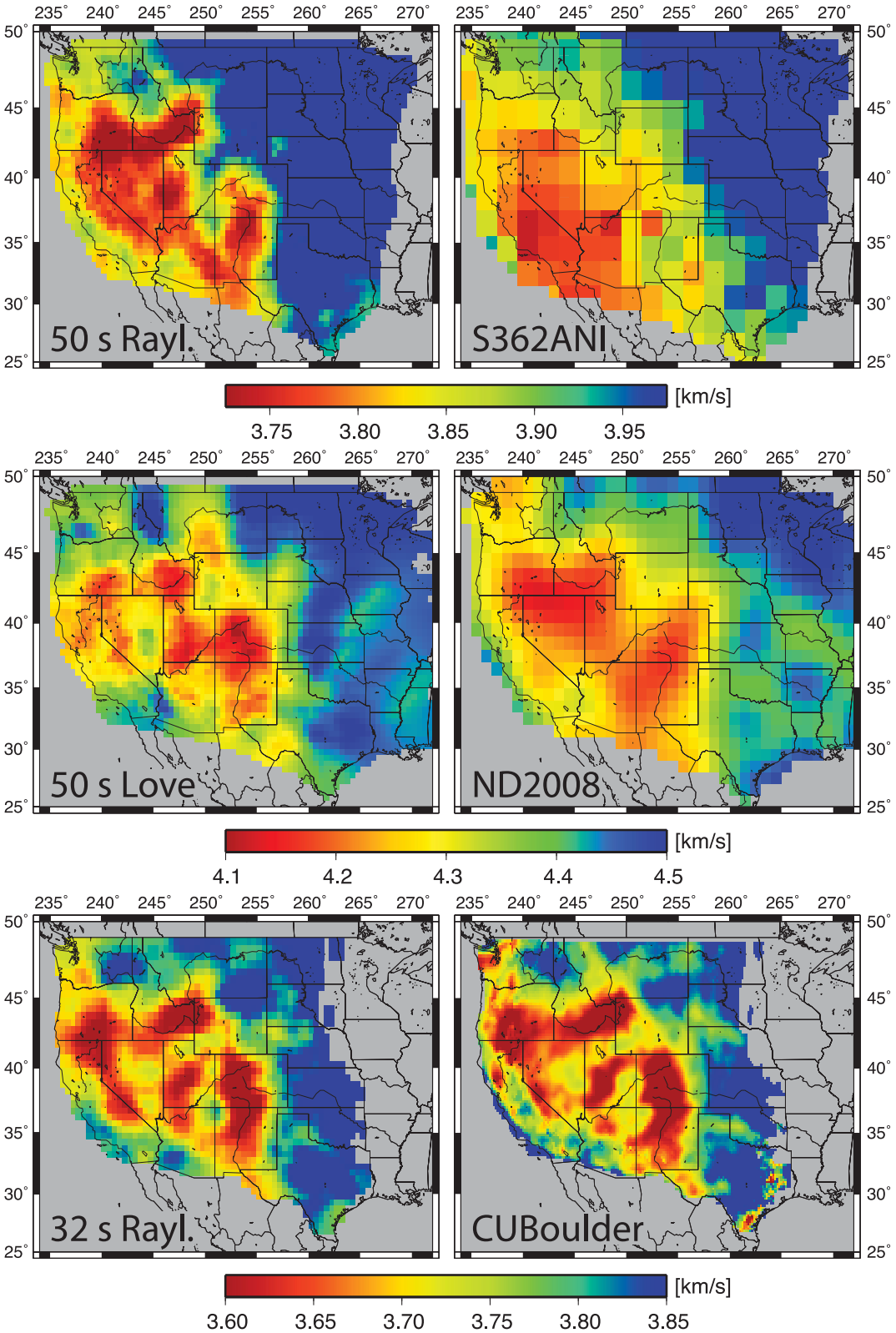

Figure 13. Comparison between this study (left) and published studies (right). Top: 50-s Rayleigh wave model from this study and the phase velocity model derived from S362ANI and CRUST 2.0 (sampled at 2° × 2° pixels). Middle: 50-s Love wave model from this study and the phase velocity model associated with the study of Nettles and Dziewoński (2008; sampled at 1° × 1° pixels). Bottom: 32-s Rayleigh wave model from this study and from the University of Colorado at Boulder (Lin *et al.* 2009), which uses measurements of ambient seismic noise (0.2° × 0.2° pixels). At each period, the models are plotted for shared pixels only.

Downloaded from http://gji.oxfordjournals.org/ at Columbia University on February 8, 2014

sediments and upper, middle and lower crust. We calculate phase velocities from these models using local depth profiles. An example is shown in the top row of Fig. 13, for Rayleigh waves at 50 s. We find that the long-wavelength structure from the global model is also well recovered in our model; however, there are notable differences at the pixel scale. These differences are primarily due to the lack of spatial resolution of mantle structure in the global model. A good example of this is the Yellowstone hotspot, a strong, short-wavelength, slow mantle feature that is not resolved in S362ANI. Short-wavelength structure in the global phase velocity map originates from CRUST 2.0. The correlation between the two models shown is 86.5 per cent. Similar correlations are found for both Love and Rayleigh waves at periods of 50 s or longer. At periods shorter than 50 s, the phase velocity structure in the two models is different, owing to the lack of smaller scale structure in the global model.

The second comparison study, that of Nettles & Dziewoński (2008, ND2008), finds the radially anisotropic shear velocity structure of North America with a resolution of a few hundred kilometres while simultaneously inverting for lower resolution global structure. This focused study with variable resolution provides improved constraints on continental-scale structure over a low-resolution global study. The associated phase velocity map for 50-s Love waves (Nettles 2005) is compared with our results in Fig. 13. We find that the long-wavelength signal present in ND2008 is captured by our regional study, with increased detail in the extent and magnitudes of the anomalies in our maps. This is particularly apparent in the Basin and Range, where we observe a ring of slow velocities enclosing the Basin and Range in our study, but a broad, lower amplitude low-velocity anomaly is seen in ND2008. The correlation value is 86.5 per cent. Analogous effects are observed at other periods and for Rayleigh wave phase-velocity maps, with correlation values ranging from 77 per cent for 35-s Love waves to 91 per cent for 50-s Rayleigh waves.

The third study we use for comparison is a regional phase velocity model derived using USArray TA data by Lin *et al.* (2009). This study uses the method of Eikonal tomography, in which recordings of ambient seismic noise are cross-correlated to compute the empirical Green's function and phase traveltimes (Lin *et al.* 2008). These measurements are interpolated to form a phase traveltime surface on a $0.2^\circ \times 0.2^\circ$ grid, which is then related to the local phase speed and direction of wave propagation using the Eikonal equation. In comparing our 32-s Rayleigh wave models (Fig. 13), we see that the two models are highly consistent despite the lower resolution in our study ($0.5^\circ \times 0.5^\circ$), with correlation values of 89.4 per cent, calculated using the models sampled at the centre of every pixel of Lin *et al.* (2009). Differences arise where Lin *et al.* (2009) resolve very short-wavelength features, on the order of the station spacing (70 km). The strength of the heterogeneity is also very similar between the models. Many velocity anomalies, such as the one located near the Rio Grande Rift (Fig. 14), show very little difference. The largest differences in strength of velocity anomalies, such as at Yellowstone hotspot, are less than 0.1 km s^{-1}. At shorter periods, the phase velocity maps show similar correlations of 88–90 per cent, and higher correlations are found with the longer periods models of Lin & Ritzwoller (2011), derived using Helmholtz tomography.

In all cases, the study with higher resolution has a slightly larger velocity range, as might be expected, but the differences in the strength of heterogeneity are small. Based on these comparisons, recent global and regional models of the Western United States are overall consistent, with the regional models and TA data providing additional information on short-wavelength structure. Regional results from different methods are also quite consistent, bringing the seismological community close to obtaining a consensus on Rayleigh wave phase velocity structure in the Western United States. Very few Love wave models from TA data have been published; the Love wave results from this study help fill the knowledge gap for smaller scale Love wave phase velocity structure of the Western United States.

5.3 Geological features

Surface waves are sensitive to intrinsic velocity structure over a range of depths. For this reason, anomalies cannot be interpreted directly in terms of heterogeneity at depth. However, many anomalies colocate with geological features (Fig. 14) in the depth range of their maximum sensitivity.

For example, in the 25-s Rayleigh wave phase velocity model (Fig. 10), phase velocities are mainly representative of lower crustal and uppermost mantle velocity structure. Slow anomalies are colocated with the Yellowstone hotspot and the Snake River Plain, as well as in the vicinity of the High Lava Plains. Slow anomalies are also associated with the edges of the Basin and Range extensional province, notably along the western edge adjacent to the Sierra Nevada mountain range, and the eastern edge, extending through the Wasatch Front and the transition to the western Colorado Plateau. These areas are the most seismically active portions of the Basin and Range (Pancha *et al.* 2006). In the northern Basin and Range, two small high-velocity anomalies appear in the same location as areas of thinned crust (Klemperer *et al.* 1986). On the eastern edge of the Colorado Plateau, slow anomalies are located along the northern Rio Grande Rift, extending northward beneath the Rocky Mountains in Colorado, possibly reflecting the velocity contrast between the deeper crustal root of the Rockies and nearby upper-mantle velocities.

There does not appear to be a coherent velocity anomaly that can be associated with the subduction of the Juan de Fuca Plate in Cascadia; instead, we see a moderately low-velocity anomaly at approximately 47°N, flanked by average velocities to the south and north. This is consistent with a regional shear wave velocity study, that finds low velocities extending to the east at 47°N at shallow depths, 4–16 km, underlain by faster material presumed to be the Juan de Fuca slab (Calkins *et al.* 2011). These features are adjacent to a high-velocity anomaly colocated with the Columbia River flood basalts to the east in Washington state.

Fast anomalies are observed in the Great Valley region, which has been interpreted as fast oceanic crust (Godfrey *et al.* 1997), and along the southwestern edge of the study region, which comprises the southern Basin and Range and northern tip of the Gulf of California. The thinned crust in this region may contribute to the fast velocity anomaly (Lewis *et al.* 2001). Finally, the entire eastern edge of the study area shows high velocities, likely representing the western edge of the North American craton.

At 50-s period, slow Rayleigh wave anomalies cover the extent of the Basin and Range, an area characterized by medium-to-high heat flow (Lysak 1992). The strongest slow anomalies align with the Yellowstone hotspot, the Snake River Plain, the High Lava Plains and the Rio Grande Rift. At this period, Rayleigh waves are primarily sensitive to the upper mantle, and any reduced velocity signal from the root of the Rocky Mountains is no longer apparent. Fast regions are located along the eastern edge of the study area, following the edge of the craton. At 100-s period, which corresponds to a maximum sensitivity at approximately 150-km depth, the dominant contrast is between slow velocities in the non-cratonic Western

Downloaded from http://gji.oxfordjournals.org/ at Columbia University on Februar

Figure 14. Topographic map showing major geological provinces: Coast Range, Cascade Ranges, Columbia Plateau flood basalts, HLP and NW B&R (High Lava Plains and Northwest Basin and Range), SRP (Snake River Plain), YS (Yellowstone), NE B&R (Northeast Basin and Range), Rocky Mountains, Great Plains, RGR (Rio Grande Rift), Colorado Plateau, WF (Wasatch Front), Southern Basin and Range, Great Basin and Northern Basin and Range, Sierra Nevada, Great Valley. Topography from GeoMapApp; geological provinces after Simpson & Anders (1992).

United States and fast velocities in the craton to the east. The exception to this first-order trend is the moderate velocities observed beneath the Columbia River flood basalt province.

Love wave phase velocities provide a different perspective on the velocity structure, with greater sensitivity to crustal structure at all periods. At short periods (25–35 s), many of the same features discussed in the Rayleigh wave models are observed. The strongest low-velocity anomaly is located in the northern Rio Grande Rift/southern Rocky Mountain region. Slow anomalies are present in the area of the Yellowstone hotspot and ringing the Basin and Range. Fast anomalies are observed in the Columbia River flood basalts and the northeastern portion of the study area. There is a fast anomaly in the southwestern region of the study area adjacent to the Gulf of California, which may correspond to the aforementioned region of thinned crust. And finally, a slow anomaly on the Gulf Coast of Texas is prominent in the Love wave models, likely caused by the thick sediments there (McGookey 1975).

The 50-s period Love wave model is very similar to the 25-s Rayleigh wave model. Slow anomalies are colocated with the Colorado Plateau, possibly reflecting the thicker crust underlying this geological feature (Zandt *et al.* 1995). Slow anomalies are also observed in the regions of the Snake River Plain, High Lava Plains and around the edges of the Basin and Range, including the Sierra Nevada. Fast anomalies are again found near the Gulf of California, the eastern edge of the study area and the northern Cascades.

At 100-s period, Love wave phase velocity anomalies map the transition between the Basin and Range and cratonic North America even more sharply than the Rayleigh wave anomalies do. The slowest velocities are found along the Rio Grande Rift, Colorado Plateau and in the northern Basin and Range. The fast anomaly observed in the northern Cascades at 50 s persists at 100 s, suggesting that it may be associated with the subducted Juan de Fuca Plate.

6 CONCLUSIONS

A two-station phase velocity measurement method that accounts for arrival-angle variations is described and tested using USArray data for the Western United States. This method cancels some sources of data uncertainty associated with the single-station method, and, therefore, makes possible investigations of smaller phase delay signals. The two-station observations are used to map Love and Rayleigh wave phase velocities between 25 and 100 s at a uniform resolution of approximately 200 km across the TA footprint. Arrival-angle corrections have modest, but systematic, effects on the final Rayleigh wave maps, and lead to an increase in the reduction of variance, reflecting more consistency in the measurements.

Analysis of the Love wave data is more challenging. The original single-station data set is smaller owing to higher noise levels on the horizontal components. In addition, the reduction in measurement uncertainty associated with construction of two-station observations is smaller than that seen for Rayleigh waves. Local phase velocity estimates for Love waves are unusually high in comparison with two-station phase velocity estimates. We speculate that the effect of overtone interference is exacerbated by the mini array measurement method. As a result, we choose not to apply the arrival-angle corrections to the Love wave measurements until undertaking further study of these effects.

Despite these difficulties, the preferred phase velocity models for both Love and Rayleigh waves are well constrained and

Downloaded from http://gji.oxfordjournals.org/ at Columbia University on February 8, 2014

provide good fits to the data. This is due in large part to the grid of the TA, which allows for even path coverage, in both area and the range of path lengths, and effective azimuthal averaging. In addition, the dense nature of the grid allows the calculation of arrival-angle estimates and associated local phase velocity measurements, which provide independent information in addition to their utility in correcting the two-station measurements. The final phase velocity models contain anomalies that compare well with both geological features and with other published studies of the Western United States. The Love and Rayleigh wave phase velocity maps developed here provide constraints for future studies of the radially anisotropic 3-D structure of North America.

The data and the models presented in this study are available at: www.ldeo.columbia.edu/~afoster/research.html (last accessed 21 November 2013).

ACKNOWLEDGEMENTS

The seismic waveforms used in this study come from the USArray component of the EarthScope facility. We are grateful to everyone involved in the operation and distribution of data from the Transportable Array and the regional networks that contribute to USArray. We thank the IRIS Data Management Center for providing excellent and robust methods of access to these data. We thank Associate Editor Gabi Laske, Toshiro Tanimoto and an anonymous reviewer for helpful comments on the manuscript. This research was funded by the National Science Foundation award EAR-0952285.

REFERENCES

Alsina, D., Snieder, R. & Maupin, V., 1993. A test of the great circle approximation in the analysis of surface waves, *Geophys. Res. Lett.,* **20**(10), 915–918.

Bassin, C., Laske, G. & Masters, G., 2000. The current limits of resolution for surface wave tomography in North America, *EOS, Trans. Am. geophys. Un.,* **81**(48), Fall Meet. Suppl., Abstract S12A-03.

Becker, T.W., Kellogg, J.B., Ekström, G. & O'Connell, R.J., 2003. Comparisons of azimuthal seismic anisotropy from surface waves and finite strain from global mantle-circulation models, *Geophys. J. Int.,* **155,** 696–714.

Beghein, C., Snoke, J.A. & Fouch, M.J., 2010. Depth constraints on azimuthal anisotropy in the Great Basin from Rayleigh-wave phase velocity maps, *Earth planet. Sci. Lett.,* **289,** 457–478.

Bensen, G., Ritzwoller, M. & Yang, Y., 2009. A 3-D shear velocity model of the crust and uppermost mantle beneath the United States from ambient seismic noise, *Geophys. J. Int.,* **177,** 1177–1196.

Bloch, S. & Hales, A., 1968. New techniques for the determination of surface wave phase velocities, *Bull. seism. Soc. Am.,* **58**(3), 1021–1034.

Boore, D., 1969. Effect of higher mode contamination on measured Love wave phase velocities, *J. geophys. Res.,* **74**(27), 6612–6616.

Boschi, L., Becker, T.W., Soldati, G. & Dziewoński, A.M., 2006. On the relevance of Born theory in global seismic tomography, *Geophys. Res. Lett.,* **33,** doi:10.1029/2005GL025063.

Brisbourne, A.M. & Stuart, G.W., 1998. Shear-wave velocity structure beneath North Island, New Zealand, from Rayleigh-wave interstation phase velocities, *Geophys. J. Int.,* **133**(1), 175–184.

Brune, J. & Dorman, J., 1963. Seismic waves and earth structure in the Canadian shield, *Bull. seism. Soc. Am.,* **53**(1), 167–210.

Calkins, J.A., Abers, G.A., Ekström, G., Creager, K.C. & Rondenay, S., 2011. Shallow structure of the Cascadia subduction zone beneath western Washington from spectral ambient noise correlation, *J. geophys. Res.,* **116,** doi:10.1029/ 2010JB007657.

Dziewonski, A. & Anderson, D., 1981. Preliminary Reference Earth Model (PREM), *Phys. Earth planet. Inter.,* **25,** 289–325.

Dziewonski, A.M. & Woodward, R., 1992. Acoustic imaging at the planetary scale, in *Acoustical Imaging,* Vol. 19, pp. 785–797, eds Ermert, H. & Harjes, H.-P., Plenum.

Ekström, G., 2011. A global model of Love and Rayleigh surface wave dispersion and anisotropy, 25-250 s, *Geophys. J. Int.,* **187,** 1668–1686.

Ekström, G., Tromp, J. & Larson, E. W.F., 1997. Measurements and global models of surface wave propagation, *J. geophys. Res.,* **102**(B4), 8137–8157.

Evernden, J.F., 1954. Direction of approach of Rayleigh waves and related problems (Part II), *Bull. seism. Soc. Am.,* **44,** 159–184.

Forbriger, T., 2003. Inversion of shallow-seismic wavefields: I. Wavefield transformation, *Geophys. J. Int.,* **153,** 719–734.

Forsyth, D., 1975. A new method for the analysis of multi-mode surface-wave dispersion: application to Love-wave propagation in the East Pacific, *Bull. seism. Soc. Am.,* **65,** 323–342.

Forsyth, D.W. & Li, A., 2005. Array analysis of two-dimensional variations in surface wave phase velocity and azimuthal anisotropy in the presence of multipathing interference, in *Seismic Earth: Array Analysis of Broadband Seismograms, 2005,* Vol. 157, pp. 81–97, eds Levander, A. & Nolet, G., American Geophysical Union.

Godey, S., Snieder, R., Villaseñor, A. & Benz, H.M., 2003. Surface wave tomography of North America and the Caribbean using global and regional broad-band networks: phase velocity maps and limitations of ray theory, *Geophys. J. Int.,* **152,** 620–632.

Godfrey, N., Beaudoin, B., Klemperer, S. & Group, M.W., 1997. Ophiolitic basement to the Great Valley forearc basin, California, from seismic and gravity data: implications for crustal growth at the North American continental margin, *Geol. soc. Am. Bull.,* **109**(12), 1536–1562.

Kimman, W., Campman, X. & Trampert, J., 2011. Characteristics of seismic noise and the average velocity structure beneath the Annerveen Gasfield, the Netherlands, in *Abstract C018 presented at 73rd European Association of Geoscientists and Engineers Conference and Technical Exhibition*, Vienna.

Klemperer, S.L., Hauge, T., Hauser, E., Oliver, J. & Potter, C., 1986. The Moho in the northern Basin and Range province, Nevada, along the COCORP 40°N seismic-reflection transect, *Geol. soc. Am. Bull.,* **97**(5), 603–618.

Knopoff, L., Mueller, S. & Pilant, W.L., 1966. Structure of the crust and upper mantle in the Alps from the phase velocity of Rayleigh waves, *Bull. seism. Soc. Am.,* **56,** 1009–1044.

Kustowski, B., Ekström, G. & Dziewoński, A.M., 2008. Anisotropic shear-wave velocity structure of the Earth's mantle: a global model, *J. geophys. Res.,* **113,** doi:10.1029/2007JB005169.

Larson, E.W.F. & Ekström, G., 2002. Determining surface wave arrival angle anomalies, *J. geophys. Res.,* **107**(B6), doi:10.1029/2000JB000048.

Laske, G., Masters, G. & Zurn, W., 1994. Frequency-dependent polarization measurements of long-period surface waves and their implications for global phase-velocity maps, *Phys. Earth planet. Inter.,* **84,** 111–137.

Lee, W.B. & Solomon, S.C., 1979. Simultaneous inversion of surface-wave phase velocity and attenuation: Rayleigh and Love waves over continental and oceanic paths, *Bull. seism. Soc. Am.,* **69**(1), 65–95.

Lerner-Lam, A.L. & Park, J.J., 1989. Frequency-dependent refraction and multipathing of 10-100 second surface waves in the Western Pacific, *Geophys. Res. Lett.,* **16**(6), 527–530.

Lewis, J.L. *et al.*, 2001. Crustal thickness of the Peninsular Ranges and Gulf Extensional Province in the Californias, *J. geophys. Res.,* **106**(B7), 13 599–13 611.

Liang, C. & Langston, C.A., 2009. Wave gradiometry for USArray: Rayleigh waves, *J. geophys. Res.,* **114,** doi:10.1029/2008JB005918.

Lin, F., Ritzwoller, M.H. & Snieder, R., 2009. Eikonal tomography: surface wave tomography by phase-front tracking across a regional broad-band seismic array, *Geophys. J. Int.,* **177**(3), doi:10.1111/j.1365-246X.2009.04105.x.

Lin, F.-C. & Ritzwoller, M.H., 2010. Empirically determined finite frequency sensitivity kernels for surface waves, *Geophys. J. Int.,* **182,** 923–932.

Lin, F.-C. & Ritzwoller, M.H., 2011. Helmholtz surface wave tomography for isotropic and azimuthally anisotropic structure, *Geophys. J. Int.,* **186,** 1104–1120.

Downloaded from http://gji.oxfordjournals.org/ at Columbia University on Februar

Lin, F.-C., Moschetti, M.P. & Ritzwoller, M.H., 2008. Surface wave tomography of the western United States from ambient seismic noise: Rayleigh and Love wave phase velocity maps, *Geophys. J. Int.,* **173,** 281–298.

Lysak, S., 1992. Heat flow variations in continental rifts, *Tectonophysics,* **208,** 309–323.

Marone, F. & Romanowicz, B., 2007. The depth distribution of azimuthal anisotropy in the continental upper mantle, *Nature,* **447,** 198–201.

Marone, F., Gung, Y. & Romanowicz, B., 2007. Three-dimensional radial anisotropic structure of the North American upper mantle from inversion of surface waveform data, *Geophys. J. Int.,* **171,** 206–222.

McGookey, D.P., 1975. Gulf Coast Cenozoic sediments and structure: an excellent example of extra-continental sedimentation, *Gulf Coast Assoc. Geol. Soc. Trans.,* **25**(197), 104–120.

Meier, T., Lebedev, S., Nolet, G. & Dahlen, F., 1997. Diffraction tomography using multimode surface waves, *J. geophys. Res.,* **102**(B4), 8255–8267.

Moschetti, M.P., Ritzwoller, M., Lin, F.-C. & Yang, Y., 2010. Seismic evidence for widespread western-US deep-crustal deformation caused by extension, *Nature,* **464,** 885–890.

Nakanishi, I. & Anderson, D., 1983. Measurements of mantle wave velocities and inversion for lateral heterogeneity and anisotropy: 1. Analysis of great circle phase velocities, *J. geophys. Res.,* **88**(B12), 10 267–10 283.

Nettles, M., 2005. Anisotropic velocity structure of the mantle beneath North America, *PhD thesis,* Harvard University.

Nettles, M. & Dziewoński, A.M., 2008. Radially anisotropic shear velocity structure of the upper mantle globally and beneath North America, *J. geophys. Res.,* **113**(B02303), doi:10.1029/2006JB004819.

Nettles, M. & Dziewoński, A.M., 2011. Effect of higher-mode interference on measurements and models of fundamental-mode surface-wave dispersion, *Bull. seism. Soc. Am.,* **101**(5), 2270–2280.

Pancha, A., Anderson, J.G. & Kreemer, C., 2006. Comparison of seismic and geodetic scalar moment rates across the Basin and Range province, *Bull. seism. Soc. Am.,* **96**(1), 11–32.

Peter, D., Tape, C., Boschi, L. & Woodhouse, J., 2007. Surface wave tomography: global membrane waves and adjoint methods, *Geophys. J. Int.,* **171,** 1098–1117.

Peter, D., Boschi, L. & Woodhouse, J., 2009. Tomographic resolution of ray and finite-frequency methods: a membrane-wave investigation, *Geophys. J. Int.,* **177**(2), 624–638.

Pilant, W.L. & Knopoff, L., 1964. Observations of multiple seismic events, *Bull. seism. Soc. Am.,* **54**(1), 19–39.

Pollitz, F.F. & Snoke, J.A., 2010. Rayleigh-wave phase-velocity maps and three-dimensional shear velocity structure of the Western US from local non-plane surface wave tomography, *Geophys. J. Int.,* **180,** 1153–1169.

Prindle, K. & Tanimoto, T., 2006. Teleseismic surface wave study for S-wave velocity structure under an array: southern California, *Geophys. J. Int.,* **166**(2), 601–621.

Satô, Y., 1955. Analysis of dispersed surface waves by means of Fourier Transform I, *Bull. Eqk. Res. Inst., Tokyo Univ.,* **33,** 33–48.

Shapiro, N.M., Campillo, M., Stehly, L. & Ritzwoller, M.H., 2005. High-resolution surface-wave tomography from ambient seismic noise, *Science,* **307**(5715), 1615–1618.

Sieminski, A., 2004. Can finite-frequency effects be accounted for in ray theory surface wave tomography?, *Geophys. Res. Lett.,* **31**(24), 1–4.

Simpson, D.W. & Anders, M.H., 1992. Tectonics and topography of the Western United States–an application of digital mapping, *GSA Today,* **2**(6), 118–121.

Spetzler, J., Trampert, J. & Snieder, R., 2002. The effect of scattering in surface wave tomography, *Geophys. J. Int.,* **149,** 755–767.

Tanimoto, T. & Prindle, K., 2007. Surface wave analysis with beamforming, *Earth Planets Space,* **59,** 453–458.

Trampert, J. & Spetzler, J., 2006. Surface wave tomography: finite-frequency effects lost in the null space, *Geophys. J. Int.,* **164,** 394–400.

Trampert, J. & Woodhouse, J.H., 1995. Global phase velocity maps of Love and Rayleigh waves between 40 and 150 seconds, *Geophys. J. Int.,* **122,** 675–690.

Tromp, J., Tape, C. & Lui, Q., 2005. Seismic tomography, adjoint methods, time reversal, and banana-donut kernels, *Geophys. J. Int.,* **160,** 195–216.

Tromp, J. *et al.*, 2010. Near real-time simulations of global CMT earthquakes, *Geophys. J. Int.,* **183**(1), 381–389.

van der Lee, S. & Frederiksen, A., 2005. Surface wave tomography applied to the North American upper mantle, in *Seismic Earth: Array Analysis of Broadband Seismograms,* pp. 67–80, eds Levander, A. & Nolet, G., Geophysical Monograph.

van der Lee, S. & Nolet, G., 1997. Upper mantle S velocity structure of North America, *J. geophys. Res.,* **102**(B10), 22 815–22 838.

Vidale, J.E., 1986. Complex polarization analysis of particle motion, *Bull. Seism. soc. Am.,* **76**(5), 1393–1405.

Wielandt, E., 1993. Propagation and structural interpretation of non-plane waves, *Geophys. J. Int.,* **113**(1), 45–53.

Woodhouse, J. & Girnius, T., 1982. Surface-waves and free oscillations in a regionalized earth model, *Geophys. J. R. astr. Soc.,* **68,** 653–673.

Yang, Y. & Forsyth, D.W., 2006. Regional tomographic inversion of the amplitude and phase of Rayleigh waves with 2-D sensitivity kernels, *Geophys. J. Int.,* **166**(3), 1148–1160.

Yao, H., van der Hilst, R.D. & de Hoop, M.V., 2006. Surface-wave array tomography in SE Tibet from ambient seismic noise and two-station analysis - I. Phase velocity maps, *Geophys. J. Int.,* **166,** 732–744.

Yoshizawa, K. & Ekström, G., 2010. Automated multimode phase speed measurements for high-resolution regional-scale tomography: application to North America, *Geophys. J. Int.,* **183,** 1538–1558.

Yoshizawa, K. & Kennett, B., 2005. Sensitivity kernels for finite-frequency surface waves, *Geophys. J. Int.,* **162**(3), 910–926.

Yoshizawa, K. & Kennett, B.L.N., 2002. Determination of the influence zone for surface wave paths, *Geophys. J. Int.,* **149,** 440–453.

Yuan, H., Romanowicz, B., Fischer, K.M. & Abt, D., 2011. 3-D shear wave radially and azimuthally anisotropic velocity model of the North American upper mantle, *Geophys. J. Int.,* **184,** 1237–1260.

Zandt, G., Myers, S.C. & Wallace, T.C., 1995. Crust and mantle structure across the Basin and Range—Colorado Plateau boundary at 37°N latitude and implications for Cenozoic extensional mechanism, *J. geophys. Res.,* **100**(B6), 10 529–10 548.

Zhou, Y., Dahlen, F. & Nolet, G., 2004. Three-dimensional sensitivity kernels for surface wave observables, *Geophys. J. Int.,* **158,** 142–168.

Zhou, Y., Nolet, G., Dahlen, F.A. & Laske, G., 2005. Finite-frequency effects in global surface-wave tomography, *Geophys. J. Int.,* **163,** 1087–1111.

Downloaded from http://gji.oxfordjournals.org/ at Columbia University on February 8, 2014